Global spatial deconvolution of Lunar Prospector Th abundances

D. J. Lawrence,[1] R. C. Puetter,[2,3] R. C. Elphic,[1] W. C. Feldman,[1] J. J. Hagerty,[1] T. H. Prettyman,[1] and P. D. Spudis[4]

Received 20 October 2006; revised 19 December 2006; accepted 4 January 2007; published 7 February 2007.

[1] We have completed the first global spatial deconvolution analysis of planetary gamma-ray data for lunar Th abundances as measured by the Lunar Prospector Gamma-ray Spectrometer. We tested two different spatial deconvolution techniques – Jansson's method and the Pixon method – and determined that the Pixon method provides superior performance. The final deconvolved map results in a spatial resolution improvement of a factor of 1.5–2. The newly deconvolved data allow us to clearly delineate nearside Th enhancements and depressions, validate enhanced Th abundances associated with specific lunar red spots, and reveal new details of the Th distribution at the Aristarchus plateau. **Citation:** Lawrence, D. J., R. C. Puetter, R. C. Elphic, W. C. Feldman, J. J. Hagerty, T. H. Prettyman, and P. D. Spudis (2007), Global spatial deconvolution of Lunar Prospector Th abundances, *Geophys. Res. Lett.*, *34*, L03201, doi:10.1029/2006GL028530.

1. Introduction

[2] The global distribution of lunar Th abundances measured by the Lunar Prospector Gamma-ray Spectrometer (LP-GRS) [*Lawrence et al.*, 1998, 2003] has significantly enhanced our understanding of the Moon's formation and evolution [*Jolliff et al.*, 2006]. For example, *Jolliff et al.* [2000] used global Th data to suggest that instead of the mare/highlands dichotomy, the Moon should be thought of as three geochemical provinces comprised of a nearside high-Th terrane, a low-Th feldspathic highlands terrane, and the South Pole-Aitken basin floor. While the LP-GRS data have shed new light on large scale lunar geochemistry, the characteristically broad spatial resolution (45 km intrinsic spatial resolution; 80 km for the smoothed Th data, *Lawrence et al.* [2003]), makes it difficult to determine the Th abundances of small-scale geologic features. To address this issue, forward modeling techniques have been used to improve our understanding of the Th abundances of small features [*Lawrence et al.*, 2003, 2005; *Hagerty et al.*, 2006]. However, these methods rely on other sources of data and it is desirable to achieve improved spatial resolution entirely internal to the LP dataset.

[3] Spatial deconvolution offers a way to improve the spatial resolution of the LP dataset if the spatial response function and statistical uncertainties of the data are sufficiently well known. Previous studies have carried out spatial deconvolution for Apollo gamma-ray, Lunar Prospector gamma-ray and neutron, and Mars Odyssey neutron data [e.g., *Haines et al.*, 1978; *Elphic et al.*, 2005; *Prettyman et al.*, 2005]. Here, we present the first results of a study where we compare two different deconvolution techniques – Jansson's method and the Pixon method – using LP-GRS Th data. We conclude that the Pixon method produces significantly improved deconvolved maps, which we use to revisit geologically complex regions, such as the Aristarchus Plateau.

2. Spatial Deconvolution Techniques

[4] Spatial deconvolution is a well-developed technique that dates back to the early 1900s [*Van Cittert*, 1931]. There exist many reviews of spatial deconvolution that are useful for understanding the various techniques [e.g., *Jansson*, 1997a; *Puetter et al.*, 2005, and references therein]. For our purpose, we define the objective of spatial deconvolution as enhancing the spatial contrast, resolution, and information density of image data to the limit allowed by the uncertainty of the data.

[5] Jansson's method [*Jansson*, 1997b] is an iterative technique that uses the following relation: $I^{(k+1)} = I^{(k)} + r(I^{(k)})(D - P \otimes I^{(k)})$. Here D is the measured Th distribution, $I^{(k)}$ is the kth iterate of the solution image, and P is the spatial response function of the Th measurement, in effect the point spread function of the LP-GRS instrument. The operator $\otimes$ is the convolution operator such that $P \otimes I = \int P(\mathbf{x} - \mathbf{y})\, I(\mathbf{y}) d\mathbf{y}$, where $\mathbf{x}$ is a vector that represents the two-dimensional position within an image array. The integral is carried out over all space where the spatial response function is non-zero. The function $r(I^{(k)})$ is a relaxation function [*Jansson*, 1997b, equation (22)] that ensures the solution stays within reasonable bounds.

[6] Jansson's method has the advantage that it is easy to implement in a simple analysis program. Furthermore, it has been shown to give reasonable results with real neutron and gamma-ray data [*Elphic et al.*, 2005; *Prettyman et al.*, 2006; *Lawrence et al.*, 2006] by suppressing many of the artifacts that can emerge with other schemes such as the Van Cittert method [*Jansson*, 1997b]. In practice, the iterations are performed to the point where the residuals map has the same statistical spread as the noise estimates of the original data. Proceeding further overfits the data and risks significant amplification of noise.

[7] The second technique we used is the spatially adaptive, image restriction method known as Pixon [*Pina and Puetter*, 1993; *Puetter*, 1995; *Puetter and Yahil*, 1999]. The Pixon method is one of a class of deconvolution techniques that seek the smoothest possible image as constrained by both the original data and the data uncertainty (or noise). A unique

[1]Group ISR-1, Los Alamos National Laboratory, Los Alamos, New Mexico, USA.
[2]Center for Astrophysics and Space Sciences, University of California, San Diego, La Jolla, California, USA.
[3]PixonImaging LLC, San Diego, California, USA.
[4]Johns Hopkins University Applied Physics Laboratory, Laurel, Maryland, USA.

0094-8276/07/2006GL028530$05.00

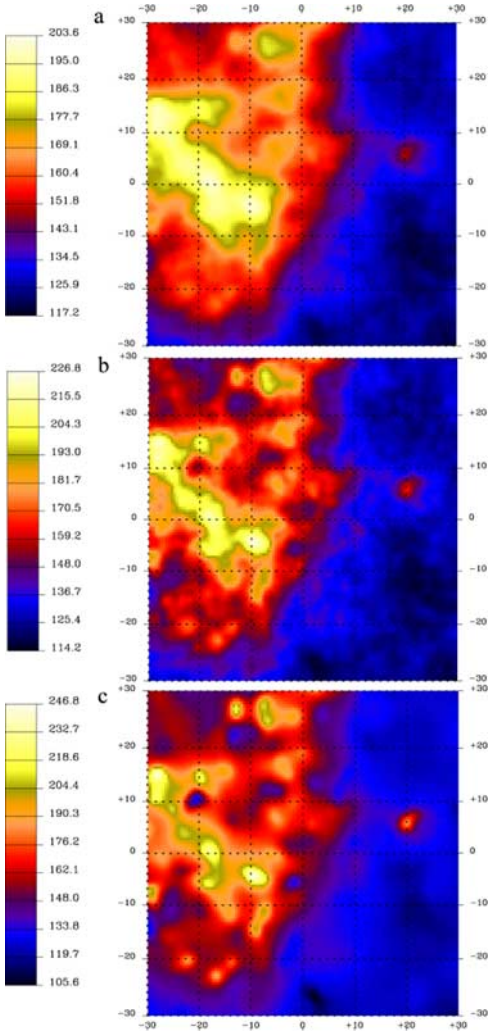

Figure 1. (a) Original Th map from *Lawrence et al.* [2003] for 30°W–30°E and 30°S–30°N. (b) Deconvolved map using Jansson's method. (c) Deconvolved map using the Pixon method. All maps are given in units of counts per 32 seconds.

feature of the Pixon method is that it uses variably sized smooth patches, or Pixon elements, within the image in order to express the information content of the image. For example, if the variation within a large portion of the image can be attributed solely to noise, then the size of the Pixon element in this region would be relatively large. In contrast, regions containing statistically significant small-scale spatial variations will have smaller Pixon element sizes that capture larger amounts of information. In general, a set of Pixon elements for a given image represents the minimum set required to describe the image information content within the limits allowed by the noise [*Puetter*, 1995]. The Pixon method has been successfully used in a variety of image analysis fields, including astronomy, microscopy, and medicine (see *Puetter et al.* [2005] for a list of specific references).

3. Spatial Deconvolution Implementation and Results

[8] Figure 1a shows the lunar region (30°W–30°E, 30°S–30°N) we are using for an initial deconvolution analysis. We have chosen a restricted region to reduce the computation time that is required for a global analysis. This particular region was chosen because the large dynamic range and small spatial scale variations of the Th abundances in this area are ideal for illustrating deconvolution results [*Lawrence et al.*, 2003]. We note that the deconvolution algorithms assume the Th data are mapped onto a flat Cartesian plane instead of a spherical surface. While this approximation can result in up to a ±3% counting rate error in the final maps, approximately 98% of the pixels in the mapped region will have an error of less than ±2%. For the spatial response function, we used the kappa function that was described by equation (2) of *Lawrence et al.* [2003], where $\sigma = 22.5$ and $\kappa = 0.626$. Note that we are deconvolving Th data that were previously smoothed with the kappa function, which means that the full spatial response function used in these analyses is the original kappa function convolved with itself.

[9] We evaluate the two different spatial deconvolution algorithms using objective criteria against which results can be measured [*Puetter et al.*, 2005]. Most importantly, the normalized residuals should be consistent with the measurement uncertainties. The normalized residuals (R) are determined using the following relation: $R = (D - P \otimes I)/s$, where I is the final deconvolved image and the residuals are normalized by the data uncertainty s. For the LP-GRS Th data, it has been shown that the uncertainties are dominated by Poisson counting statistics [*Lawrence et al.*, 2000] and the uncertainties for the smoothed Th data are determined by propagation of errors [*Hagerty et al.*, 2006]. Note also that the deconvolution here is carried out using counting rates instead of Th abundances in order to more easily account for the data uncertainties.

[10] We know that there is a problem with the deconvolved map if: 1) there is spatial structure in the residuals map correlated to the original data and/or 2) the statistical distribution of the scaled residuals is inconsistent with the known uncertainties (i.e., a histogram of the residuals should be Gaussian, be centered around zero, and have a width equal to 1). Either of these situations could be caused by an incorrect spatial response function, incorrect noise model, or a non-optimal deconvolution algorithm. Visual inspection of the final deconvolved and residual maps can serve as a qualitative guide in identifying artifacts. Finally, carrying out simulations using known data is useful for exploring systematic trends in the deconvolution algorithms. Such simulations, and the fact that they further validate the analyses shown here, will be described in a more complete description of LP-GRS deconvolution studies.

[11] Figure 1b shows the deconvolution result using Jansson's method that was optimally carried out with five iterations (i.e., the width of the residual histogram was 1 for five iterations). There is a clear sharpening of the image compared to the original map. In addition, the deconvolved map resolves some small-scale features identified in other studies (see Section 4). Figures 2a and 3a show the residuals map and histogram, respectively. The residuals map shows numerous features that are spatially correlated with Th enhancements and depressions. The scaled residuals histogram is approximately Gaussian in shape, but has an enhanced tail at high values. While the width of the histogram is 1.0, the peak of the histogram is shifted to

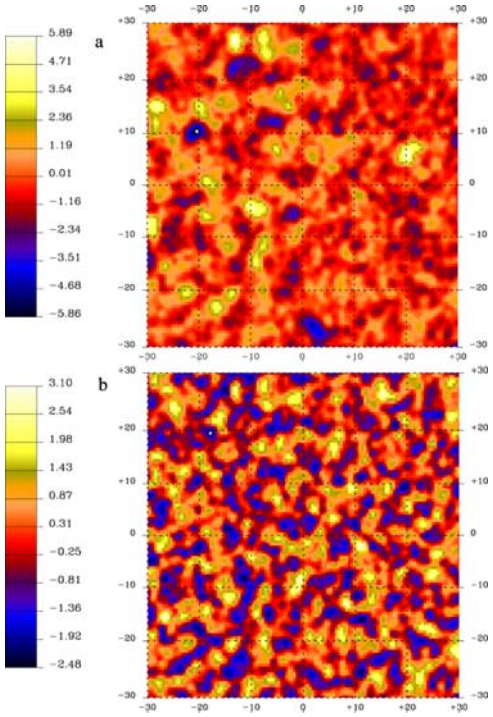

Figure 2. Residuals map from (a) Jansson's method and (b) the Pixon method.

negative values by 38% of the standard deviation. This is a significant effect, especially since this is a systematic effect and will accumulate for features extending over a number of pixels. Finally, we note that the deconvolved map shows high frequency spatial variations that are indicative of noise artifacts.

[12] Figure 1c shows the deconvolution results using the Pixon method. Many of the same features seen in Figure 1b are also seen here, but the reconstructed map is significantly smoother, which is consistent with the goal of finding the simplest image consistent with the data and uncertainties [*Puetter et al.*, 2005]. Figures 2b and 3b show the residual map and histogram for the Pixon method. Compared to Jansson's technique, the Pixon residual map is smoother and does not show the same degree of spatial correlation with the original map. The histogram of Pixon residuals shows a mostly Gaussian shape with a width (0.96) that is close to 1 and has an offset that is less than 1% of the standard deviation. This result contrasts to the Jansson histogram,

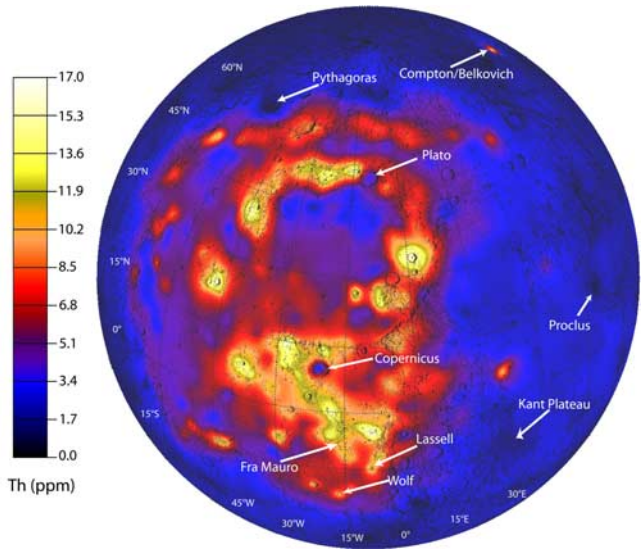

Figure 4. Nearside map of Pixon deconvolved Th abundances.

which has a significant negative offset. Both the residual map and histogram show that the Pixon method gives a result that is more consistent with the data uncertainties than is given by the Jansson result. When these criteria are combined with the observation that the Pixon map is markedly smoother than the Jansson map, we conclude that the Pixon technique gives a significantly improved result that is better than the Jansson technique, and that some of the high frequency spatial features seen in the Jansson results are artifacts and not warranted by the data.

4. Full Nearside Map and Discussion

[13] Figure 4 shows a global nearside map where the Th abundances have been deconvolved using the Pixon method. This map was constructed using ~900 × 900 km sized regions (i.e., 60° × 60° equivalent size at the equator) that were combined together to create the map shown. The absolute Th abundances were derived by correlating the deconvolved counting rate with the Th abundances of *Prettyman et al.* [2006] in a manner similar to what was done for the smoothed Th map of *Lawrence et al.* [2003].

[14] We note that there is an improvement in spatial resolution by approximately a factor of 1.5–2 over the Th map of *Lawrence et al.* [2003]. The spatial resolution was

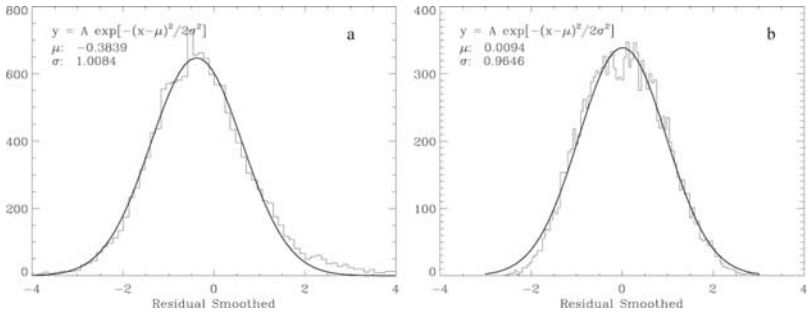

Figure 3. Residual histogram from (a) Jansson's method and (b) the Pixon method.

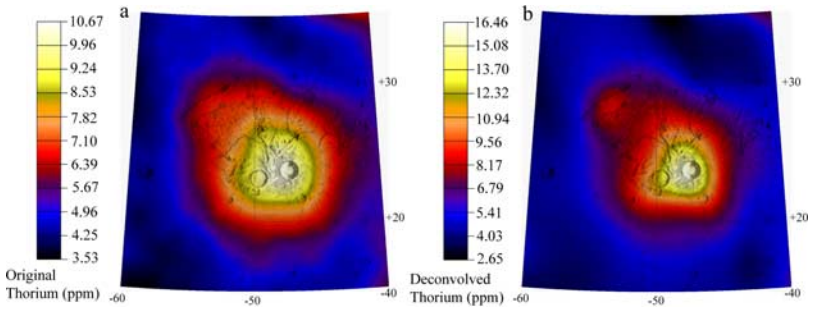

Figure 5. (a) Original Th abundances at Aristarchus crater. (b) Pixon deconvolved Th abundances at Aristarchus crater.

determined by taking profiles (not shown) across apparent point source locations (e.g., Compton Belkovich at 60°N, 100°E, Wolf crater at 23°S, 16°W) and determining the width of the profile in the deconvolved map compared to the original map. This technique indicates that the average spatial resolution of the new map is ~40–50 km, which is close to the intrinsic spatial resolution of the LP-GRS data.

[15] There are a number of features in the deconvolved map whose spatial contrast is significantly enhanced compared to the original data [*Lawrence et al.*, 2003]. For example, the craters Plato (51°N, 9°W) and Copernicus (10°N, 20°W) are clearly delineated from their surrounding regions as Th lows and these data show that the Th abundances within these craters are ~2–3 ppm compared to the >4–5 ppm values seen in the original map. There are also a number of locations in the Fra Mauro region that show strong correlation with spectrally derived, high spatial resolution FeO data [*Lucey et al.*, 2000], which provide confidence in the validity of the deconvolved data [*Lawrence et al.*, 2006].

[16] Several Th lows are found throughout the nearside area analyzed (Figure 4). In particular, we find very low Th content associated with the craters Pythagoras (63°N, 64°W), Proclus (16°N, 47°E), and the Kant Plateau (12°S, 22°E). All of these areas are known locations of deposits with very low Fe content, determined by both Clementine spectral reflectance [*Lucey et al.*, 2000] and LP-GRS Fe maps [*Lawrence et al.*, 2002]. Moreover, some of these areas are known locations of nearly pure anorthosite deposits [e.g., *Hawke et al.*, 2003]. Thus, the new deconvolved Th map is also useful for mapping and delineating the locations of ancient feldspathic crust on the Moon.

[17] The deconvolved data have also confirmed some earlier forward modeling analyses of small (<30 km) lunar features known as red spots [*Hagerty et al.*, 2006]. In particular, the new map indicates that the Gruithuisen domes (37°N, 40°W) and especially the Lassell massif (15°S, 8°W) are Th-rich features that likely have Th abundances greater than 20 ppm. The existence of these enhancements was first inferred using forward modeling techniques, but resolved spatial enhancements were not directly seen with the original Th data. We note however, that the Hansteen Alpha feature, which was inferred to have a Th abundance of ~20 ppm using forward modeling [*Lawrence et al.*, 2005; *Hagerty et al.*, 2006] is not seen as an isolated Th enhancement in the deconvolved data. Further study of this region is thus warranted to improve our understanding of its Th abundances.

[18] Finally, Figure 5 shows a regional view of the Aristarchus region. These data show a Th enhancement at Aristarchus crater (24°N, 47°W) with lower abundances to the northwest (NW) over the Aristarchus plateau. The Aristarchus plateau is covered by large expanses of pyroclastic deposits that do not appear to have analogs in the Apollo sample collection [e.g., *Shearer and Papike*, 1993]. In the deconvolved map (Figure 5b), the Th abundances in the plateau show a lane of low values co-located with a region of relatively high iron abundances (14–18 wt.% FeO) [*Lucey et al.*, 2000] that appear to be associated with the Agricola Straits. There is also a new, separate enhancement of high Th associated with the Agricola mountains. Neither the low-Th lane nor the NW enhancement were seen in the original low resolution Th data (Figure 5a). The new map shows that this NW Th enhancement is not related to Th-rich impact ejecta from Aristarchus crater and suggests that high-Th lithologies make up at least part of the Agricola mountains. The mountains appear to have 10–13 wt.% FeO, 2–4 wt.% TiO_2, and 7–9 ppm Th. Such values are consistent with mafic impact melt rocks and breccias in the lunar sample suite [*Papike et al.*, 1998, and references therein]. If, however, the Th enhancement is associated with the basalt in the Agricola Straits, the chemical composition of the basalt would be similar to KREEP basalts returned by the Apollo 15 mission [*Papike et al.*, 1998, and references therein]. Unfortunately, even with the improved spatial resolution of the new Th map, we cannot determine the Th abundances of specific geologic features in this region. However, we are in the process of forward modeling the Th abundances in this area, which will provide additional information about the Th abundance distribution of the Aristarchus plateau. We plan to use the new Th map to help unravel the geologic structure of this complex area.

[19] **Acknowledgments.** The authors thank reviewer Paul Lucey for helpful comments. This work was supported in part by NASA through Discovery Data Analysis Program grant W-7405-ENG-36 and by internal Los Alamos funding. This work was conducted under the auspices of the U. S. Department of Energy.

References

Elphic, R. C., et al. (2005), Using models of permanent shadow to constrain lunar polar water ice abundances, *Lunar Planet. Sci., XXXVI*, abstract 2297.

Hagerty, J. J., D. J. Lawrence, B. R. Hawke, D. T. Vaniman, R. C. Elphic, and W. C. Feldman (2006), Refined thorium abundances for lunar red

spots: Implications for evolved, nonmare volcanism on the Moon, *J. Geophys. Res.*, *111*, E06002, doi:10.1029/2005JE002592.

Haines, E. L., et al. (1978), Thorium concentrations in the lunar surface. II: Deconvolution modeling and its application to the regions of Aristarchus and Mare Smythii, *Proc. Lunar Planet. Sci. Conf.*, *9*, 2985.

Hawke, B. R., C. A. Peterson, D. T. Blewett, D. B. J. Bussey, P. G. Lucey, G. J. Taylor, and P. D. Spudis (2003), Distribution and modes of occurrence of lunar anorthosite, *J. Geophys. Res.*, *108*(E6), 5050, doi:10.1029/2002JE001890.

Jansson, P. A. (1997a), *Deconvolution of Images and Spectra*, Elsevier, New York.

Jansson, P. A. (1997b), Modern constrained nonlinear methods, in *Deconvolution of Images and Spectra*, pp. 107–181, Elsevier, New York.

Jolliff, B. L., J. J. Gillis, L. A. Haskin, R. L. Korotev, and M. A. Wieczorek (2000), Major lunar crustal terranes: Surface expressions and crust-mantle origins, *J. Geophys. Res.*, *105*(E2), 4197–4216.

Jolliff, B. L., et al. (Eds.) (2006), *New Views of the Moon*, *Rev. Mineral. Geochem.*, vol. 60, Mineral. Soc. of Am., Chantilly, Va.

Lawrence, D. J., et al. (1998), Global elemental maps of the Moon: The Lunar Prospector Gamma-Ray Spectrometer, *Science*, *284*, 1484–1489.

Lawrence, D. J., W. C. Feldman, B. L. Barraclough, A. B. Binder, R. C. Elphic, S. Maurice, M. C. Miller, and T. H. Prettyman (2000), Thorium abundances on the lunar surface, *J. Geophys. Res.*, *105*(E8), 20,307–20,332.

Lawrence, D. J., W. C. Feldman, R. C. Elphic, R. C. Little, T. H. Prettyman, S. Maurice, P. G. Lucey, and A. B. Binder (2002), Iron abundances on the lunar surface as measured by the Lunar Prospector gamma-ray and neutron spectrometers, *J. Geophys. Res.*, *107*(E12), 5130, doi:10.1029/2001JE001530.

Lawrence, D. J., R. C. Elphic, W. C. Feldman, T. H. Prettyman, O. Gasnault, and S. Maurice (2003), Small-area thorium features on the lunar surface, *J. Geophys. Res.*, *108*(E9), 5102, doi:10.1029/2003JE002050.

Lawrence, D. J., B. R. Hawke, J. J. Hagerty, R. C. Elphic, W. C. Feldman, T. H. Prettyman, and D. T. Vaniman (2005), Evidence for a high-Th, evolved lithology on the Moon at Hansteen Alpha, *Geophys. Res. Lett.*, *32*, L07201, doi:10.1029/2004GL022022.

Lawrence, D. J., et al. (2006), Spatial deconvolution studies of nearside Lunar Prospector thorium abundances, *Lunar Planet. Sci.*, *XVII*, abstract 1915.

Lucey, P. G., D. T. Blewett, and B. L. Jolliff (2000), Lunar iron and titanium abundance algorithms based on final processing of Clementine ultraviolet-visible images, *J. Geophys. Res.*, *105*(E8), 20,297–20,306.

Papike, J. J., G. Ryder, and C. K. Shearer (1998), Lunar samples, *Rev. Mineral.*, *36*, 5-1–5-189.

Pina, R. K., and R. C. Puetter (1993), Bayesian image reconstruction: The pixon and optimal image modeling, *Publ. Astron. Soc. Pac.*, *105*, 630–637.

Prettyman, T. H., et al. (2005), Spatial deconvolution of mars Odyssey neutron spectroscopy data: Analysis of mars southern seasonal cap, *Lunar Planet. Sci.*, *XXXVI*, abstract 1384.

Prettyman, T. H., J. J. Hagerty, R. C. Elphic, W. C. Feldman, D. J. Lawrence, G. W. McKinney, and D. T. Vaniman (2006), Elemental composition of the lunar surface: Analysis of gamma ray spectroscopy data from Lunar Prospector, *J. Geophys. Res.*, *111*, E12007, doi:10.1029/2005JE002656.

Puetter, R. C. (1995), Pixon-based multiresolution image reconstruction and the quantification of picture information content, *Int. J. Imaging Syst. Technol.*, *6*, 314–331.

Puetter, R. C., and A. Yahil (1999), The pixon method of image reconstruction, *Astron. Data Anal. Software Syst*, *172*, 307–316.

Puetter, R. C., et al. (2005), Digital image reconstruction: Deblurring and denoising, *Annu. Rev. Astron. Astrophys.*, *43*, 139–194.

Shearer, C. K., and J. J. Papike (1993), Basaltic magmatism on the Moon: A perspective from volcanic picritic glass beads, *Geochim. Cosmochim. Acta*, *57*(19), 4785–4812.

Van Cittert, P. H. (1931), Effect of slit width upon distribution of intensity in spectral lines. II, *Z. Phys.*, *69*(5–6), 298–308.

R. C. Elphic, W. C. Feldman, J. J. Hagerty, D. J. Lawrence, and T. H. Prettyman, Group ISR-1, Los Alamos National Laboratory, Group ISR-1, Los Alamos, NM 87545, USA.

R. C. Puetter, Center for Astrophysics and Space Sciences, University of California, San Diego, La Jolla, CA 92093, USA.

P. D. Spudis, Johns Hopkins University Applied Physics Laboratory, Laurel, MD 20723, USA.